Composite superplastic aerogel scaffolds containing dopamine and bioactive glass-based fibers for skin and bone tissue regeneration

Zhengchao Yuan [a,b,1], Lixiang Zhang [c,1], Muhammad Shafiq [d,1], Xinyi Wang [b], Pengfei Cai [b], Abdul Hafeez [e], Yangfan Ding [b], Zewen Wang [a], Mohamed EL-Newehy [f], Meera Moydeen Abdulhameed [f], Lianyong Jiang [g,*], Xiumei Mo [b,*], Yuan Xu [a,*]

[a] *Department of Orthopaedics, Xinqiao Hospital, Army Medical University, No. 183, Xinqiao Street, Shapingba District, Chongqing 400037, China*
[b] *State Key Laboratory for Modification of Chemical Fibers and Polymer Materials, Shanghai Engineering Research Center of Nano-Biomaterials and Regenerative Medicine, College of Biological Science and Medical Engineering, Donghua University, Songjiang, Shanghai 201600, PR China*
[c] *Department of Health Management, Characteristic Medical Center of Chinese People's Armed Police Force, 220 Chenglin Road, Hedong District, Tianjin, China*
[d] *Innovation Center of Nanomedicine, Kawasaki Institute of Industrial Promotion, Kawasaki, Kanagawa 210-0821, Japan*
[e] *Department of Mechanical Engineering, Faculty of Engineering, University of Engineering & Technology (UET), Lahore 54000, Pakistan*
[f] *Department of Chemistry, College of Science, King Saud University, P.O. Box 2455, Riyadh 11451, Saudi Arabia*
[g] *Department of Cardiothoracic Surgery, Xinhua Hospital Affiliated to Shanghai Jiao Tong University School of Medicine, Shanghai, China*

GRAPHICAL ABSTRACT
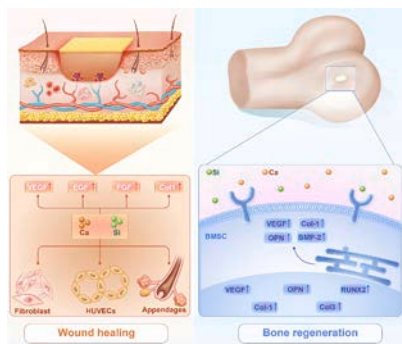
ARTICLE INFO

ABSTRACT

Multifunctional bioactive biomaterials with integrated bone and soft tissue regenerability hold great promise for the regeneration of trauma-affected skin and bone defects. The aim of this research was to fabricate aerogel scaffolds (GD-BF) by blending the appropriate proportions of short bioactive glass fiber (BGF), gelatin (Gel), and dopamine (DA). Electrospun polyvinyl pyrrolidone (PVP)-BGF fibers were converted into short BGF through calcination and homogenization. Microporous GD-BF scaffolds displayed good elastic deformation recovery and promoted neo-tissue formation. The DA could enable thermal crosslinking and enhance the mechanical properties and structural stability of the GD-BF scaffolds. The BGF-mediated release of therapeutic ions shorten hemostatic time (<30 s) in a rat tail amputation model and a rabbit artery injury model alongside inducing the

* Corresponding authors.
  E-mail addresses: jianglianyong@xinhuamed.com.cn (L. Jiang), xmm@dhu.edu.cn (X. Mo), 15123161526@163.com (Y. Xu).
[1] Z.Y., L.Z., and M.S. are the co-first authors.

Tissue repair
Regenerative medicine

regeneration of skin appendages (e.g., blood vessels, glands, etc.) in a full-thickness excisional defect model in rats (percentage wound closure: GD-BF2, 98 % *vs.* control group, 83 %) at day 14 *in vitro*. Taken together, these aerogel scaffolds may have significant promise for soft and hard tissue repair, which may also be worthy for the other related disciplines.

1. Introduction

As a dynamic load-bearing organ, bone tissues remodel throughout the life cycle displaying a certain degree of self-healing [1,2]. However, bone defects can be caused by the different types of diseases, including trauma, fracture, bone tumor, osteoporosis, skeletal malformation, and avascular necrosis [3]. Bone defects originating from trauma are often accompanied by the damage of the surrounding soft tissues. Consequently, considerable research has been carried out for the simultaneous regeneration of soft and hard tissues [4,5]. Multifunctional approaches for soft and hard tissue repair therefore may hold significant promise.

Bioactive materials offer an invaluable platform for osteochondral

tissue repair, which is ascribed to their beneficial effects on the cellular function and neo-tissue formation [6,7]. Especially, bioactive ingredients, including bioceramics, calcium phosphate, hydroxyapatite, and bioactive glass (BG) have garnered considerable attention of the research community for bone regeneration [8,9]. The BG comprised of different types of elements, such as calcium (Ca), silicon (Si), and phosphorous (P) has been shown to simultaneously induce osteogenesis and angiogenesis as well as promote cell migration [1]. Despite an obvious potential of the BG to facilitate soft and hard tissue repair, it is tedious to fully harness the therapeutic potential of the BG partly due to its fragility and poor retention at the injury site. Due to these limitations, the BG may not fully improve host-implant integration and neo-vessel
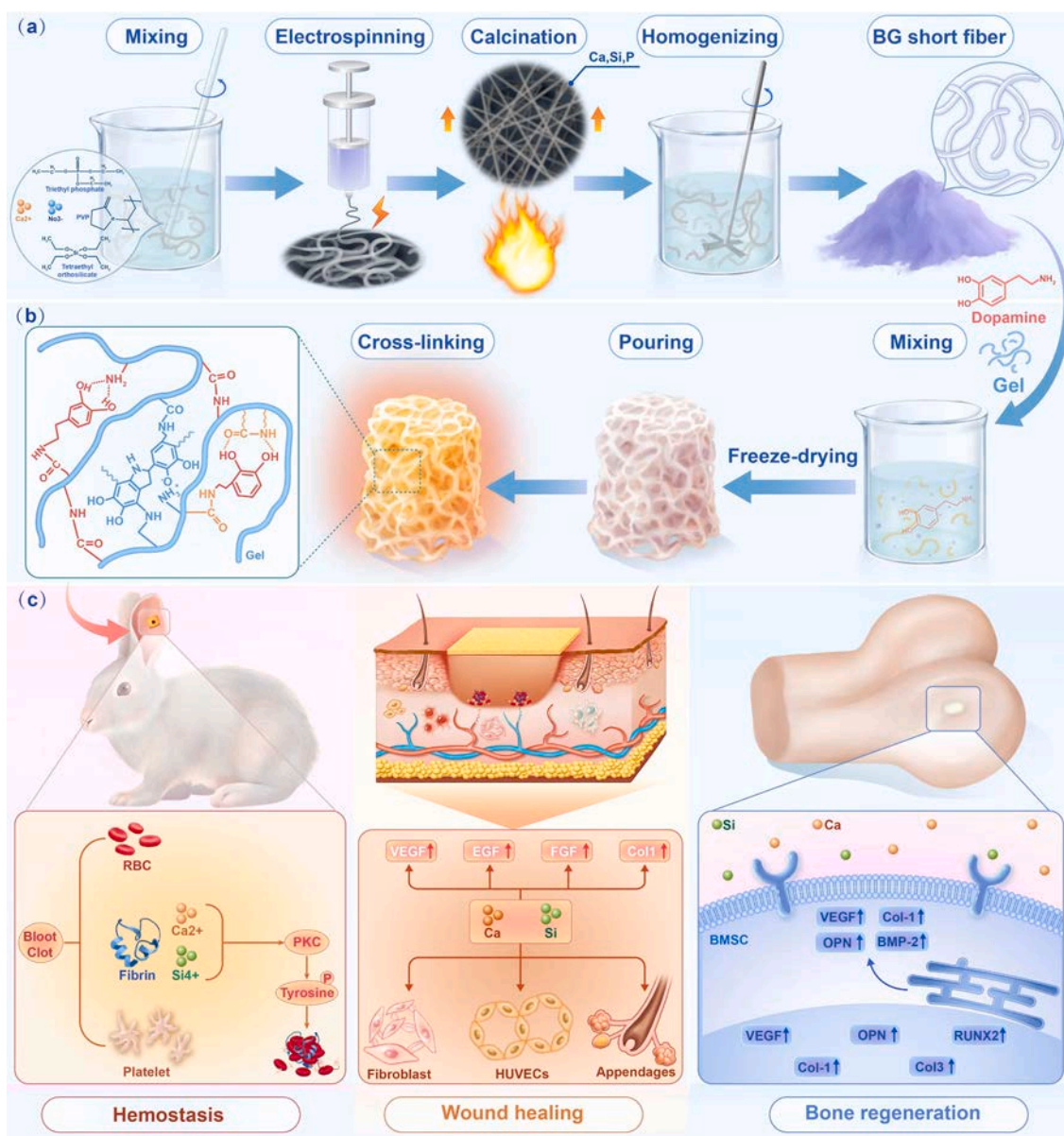
Fig. 1. Overview of the experimental design. (a) Fabrication of the BGF. (b) Fabrication of the aerogel scaffolds. (c) An illustration of the dynamic and interactive process of aerogel scaffold during hemostasis, wound healing, and bone regeneration.

formation [10].

Electrospun scaffolds may afford extracellular matrix (ECM)-mimetic morphological features as well as help disperse micro/nanomaterials for practical gains [11]. However, scaffolds assembled from electrospinning are generally two-dimensional (2D) membranes displaying densely-packed fiber layers with only superficial pores. These thick fibrous scaffolds often impede cell and tissue infiltration as well as hinder the diffusion of oxygen and the transport of nutrients, which may not be conducive for the tissue repair [12]. Therefore, it is imperative to develop three-dimensional (3D) porous scaffolds, which can simultaneously induce angiogenesis and osteogenesis. However, mere spinning of the BG alone may afford fragile fibers with insufficient mechanical properties, which may not be conducive for the bone tissue repair.

Recently, electrospinning and freeze-drying have been concurrently harnessed to fabricate 3D fiber-aerogel scaffolds (Fig. 1). These super-plastic and superabsorbent scaffolds may serve as ECM templates and offer a conducive environment for cell growth and tissue repair [1]. Similarly, organic/inorganic hybrid aerogel scaffolds have been prepared and shown to display structural and morphological features similar to the bone tissues alongside sufficient elasticity and shape-memory. These aerogel scaffolds were shown to promote osteogenesis and angiogenesis when employed for the fracture healing [1,13]. Nonetheless, these aerogel scaffolds lack microporous structure, which may not be conducive to the diffusion of oxygen as well as the transport of the nutrients [14]. Alternatively, freeze-dried scaffolds exhibit microporous structures, which may confer a conducive environment for cell growth. Therefore, the combination of fiber-aerogel scaffold and hydrogel-aerogel scaffold may be advantageous owing to their 3D morphology, porosity, and ECM-mimetic fibers' morphology.

Therefore, the objective of this study was to fabricate 3D scaffolds by co-leveraging aerogel scaffolds and hydrogels. We used gelatin (Gel) owing to its hydrophilicity and biocompatibility [15]. The BG fibers comprising of Ca, Si, and P were used to provide bioactive ingredients and therapeutic ions [16]. Short BG fibers (BGF) were prepared by electrospinning and homogenization, which were subsequently dispersed in an aqueous Gel solution containing dopamine (DA). The Gel/DA mixture containing different content of BGF was freeze-dried and thermally-crosslinked to afford BGF-aerogel scaffolds (Fig. 1a) [1,17]. The DA could promote the thermal crosslinking, thereby improving the mechanical properties and structural stability of the GD-BF scaffolds (Fig. 1b). The bioactive ingredients and therapeutic ions released by the BG could promote neovascularization and biomineralization for bone defect repair (Fig. 1c).

2. Materials and methods

2.1. Materials

Tetraethyl orthosilicate (TEOS), triethyl phosphate (TEP), dopamine (DA), and polyvinylpyrrolidone (PVP, M_w = 130 kDa) were obtained from Sigma-Aldrich, Shanghai, China. Gelatin (Gel, type B, 48722-500G-F) was purchased from MP Biomedicals, LLC (Shanghai, China). The 1,1,1,3,3,3-hexafluoro-2-propanol (HFIP) was obtained from Shanghai Darui Fine Chemical Co., Ltd. (Shanghai, China). Human umbilical vein endothelial cells (HUVECs) were obtained from the Typical Culture Collection Committee Cell Bank, Chinese Academy of Science (Shanghai, China). The rat bone marrow derived stem cells (rBMSCs) were isolated from SD rats following the previous reports [18]. Fetal bovine serum (FBS, BC-SE-FBS01) was purchased from BioChannel Biotechnology (Nanjing, China) and the Dulbecco's modified Eagle Medium (DMEM) (catalog # 11995) were obtained from Beijing Solarbio Science & Technology Co., Ltd. (Beijing, China). All other chemicals were of analytical grade and used without any further purification.

2.2. Preparation of BGF and aerogel scaffolds

2.2.1. Preparation of BG fibers

The TEOS (1.34 g), TEP (0.116 g), Ca(NO$_3$)$_2$·4H$_2$O (0.148 g), HCl (0.10 mL, 1 mol/L), and PVP (1.65 g) were dissolved in a mixture of ethanol (10.0 mL), deionized water (5 mL), and HFIP (3 mL) to afford the spinning solution [19]. The PVP-BG fibers were prepared by electrospinning (Yongkang Leye Technology Development Co., Ltd. SS-3556H, Beijing, China) using following conditions: needle size, 20G; syringe pump, 10 mL; applied voltage, 15 kV; flow rate, 1.0 mL/h; collector speed, 90 rotations per minute (rpm); and distance between the spinneret and the collector, 15 cm. To prepare BG fibers, the PVP-BG fibers were sintered in a muffle furnace (Yamato Scientific Co., Ltd, FO711, Shanghai, China) at 1,000 °C for up to 3.5 h.

2.2.2. Preparation of BGF-loaded aerogels

To fabricate BGF-loaded aerogels, DA (0.5 mg) and Gel (1 g) were dispersed into 100 mL of water to afford GD solution. Thereafter, different content of BGF (e.g., 0.5 g, 1.0 g, 1.5 g, etc.) were added into a total 100 mL of GD solution and mixed using a homogenizer (IKA T18, IKA, Germany) for up to 10 min at 8,000 rpm. The BGF suspension was poured into the mold (e.g., 48-well cell culture plate, 24-well cell culture plate, etc.), frozen at −80 °C for up to 4 h, and then freeze-dried for up to 48 h to obtain aerogel scaffolds. The aerogel scaffolds were thermally crosslinked at 190 °C in a muffle furnace (Yamato Scientific Co., Ltd, FO711, Shanghai, China) for up to 2 h. The scaffolds containing 0.5, 1.0 and 1.5 wt% (g/mL) of BGF were represented as GD-BF1, GD-BF2, and GD-BF3, respectively.

2.3. Physicochemical characterization

2.3.1. Structural analysis

The PVP-BG and BG fibers were sputter-coated with gold and their morphology was discerned by SEM (Hitachi, TM-1000, Tokyo, Japan) at an accelerating voltage of 15 kV. For the quantitative analysis of average distribution of fibers (n = 100), five different areas of a 1500X SEM micrograph were analyzed by Image J (National Institutes of Health, v1.8.0, USA). Surface morphology of fibers was assessed by scanning electron microscopy (SEM, Hitachi, TM-1000, Tokyo, Japan), while elemental mapping of carbon (C), oxygen (O), Si, Ca, and P was performed with an EDX spectrometer after gold coating (10 mA, 45 s). Surface compositions of scaffolds were analyzed using X-ray photoelectron spectroscopy (XPS, Kratos Analytical, Manchester, UK).

2.3.2. Water absorption

For water absorption, aerogel scaffolds (n = 3) were weighed in the dry state (A_0). The samples were then immersed into the phosphate-buffered saline (PBS, pH = 7.4 ± 0.1) for up to 30 min. Adsorbed water was removed using a paper towel and samples were weighted again (A_1). Maximum water absorption (MWA) was calculated using Eq. 1:

$$MWA = \frac{(A_1 - A_0)}{A_0} \times 100\% \qquad (1)$$

where A_0 and A_1 represent weight of scaffolds in the dry and wet states, respectively.

2.3.3. Mechanical testing

Mechanical properties of scaffolds were evaluated using a universal testing machine (Instron 3345, Norwood, MA, USA) with a 200-N load cell at a strain rate of 5 mm/min at room temperature (r.t.). Cylinderical scaffolds (height = 10 mm, φ = 10 mm) were soaked into the PBS for 6 h to afford wet samples for testing and were analyzed for compression strength at a compression strain of 80 %. Compressive moduli of scaffolds were measured by the slope fitting method using an initial linear

region of the stress–strain curves.

2.3.4. The release of calcium ions and degradation of aerogels in vitro

The release of calcium ions (Ca^{2+}) was studied by a calcium ion test kit (C004-2–1, Nanjing Jiancheng Institute of Biological Engineering, Nanjing, China). Samples (ca. 50 mg) were immersed into 50 mL of deionized (DI) water and stirred at 37 °C. At pre-determined time points, the concentration of calcium ions (Ca^{2+}) was analyzed by a microplate reader (Thermo Fisher Multiskan FC, Thermo Fisher Scientific, Waltham, MA, USA) at a wavelength of 610 nm following manufacturer's instructions. The detailed method for release of silicate ions (Si^{4+}) and phosphate ions (PO_4^{3-}) is described in Supplementary Information.

The degradation of scaffolds was performed using PBS. Samples (weight = 20–60 mg, $n = 5$) were weighted (B_0) and immersed in the PBS at 37 °C and 120 rpm. At pre-determined time points, samples were collected, rinsed with the DI water 3 times, freeze-dried and weighed again (B_z). The surface morphology of the well-dried samples was observed by optical microscope and SEM. The remained mass of the samples was calculated using Eq. (2):

$$\text{Remained mass} = \frac{B_z}{B_0} \times 100\% \tag{2}$$

where B_0 and B_z represent weight of samples before and after incubation into the PBS, respectively.

2.4. Biocompatibility and biological function in vitro

2.4.1. Cytocompatibility of aerogels

Scaffolds were sterilized using gamma rays (Source, Cobalt-60) for up to 6 h, washed with PBS three times, and incubated with DMEM (10 % FBS supplemented) for up to 2 h. The rBMSCs (1.4×10^4) were seeded on the scaffolds and cultured for up to 1, 3, and 7 days. DMEM high-sugar complete medium supplemented with 10 % FBS was changed every other day. Cell-seeded scaffolds were incubated at 37 °C in an incubator containing 5 % CO_2. At day 3 and 7, cell viability was examined by a live/dead cell imaging kit (Solarbio Science & Technology Co., Ltd., Beijing, China). The stained constructs were imaged using a fluorescence microscope (Eclipse TS100, Nikon, Japan). For cell proliferation, cell-seeded scaffolds were washed with PBS three times and incubated with cell counting kit (CCK-8, Beyotime, China) solution (total volume, 200 μL; serum-free medium: CCK-8 = 180: 20 μL) for up to 1 h at 37 °C. The absorbance of the solution (ca. 100 μL) was measured at 450 nm with a microplate reader (Thermo Fisher Multiskan FC, Thermo Fisher Scientific, Waltham, MA, USA).

2.4.2. Transwell migration assay in vitro

The migratory response of HUVECs and rBMSCs toward scaffolds was analyzed with a Transwell migration assay *in vitro*. Inserts containing polycarbonate membrane (pore size, 8 μm; Corning, USA) were used [20]. Sterilized scaffolds were placed into cell culture plate and incubated with the serum-free medium (ca. 500 μL) for up to 2 h. Cell suspension (ca. 200 μL, 2×10^4 cells/insert) was added into the inserts and placed into the cell culture plate along with medium and incubated at 37 °C at 5 % CO_2 for 12 h. The inserts were washed with the PBS three times and stained with crystal violet solution (ca. 500 μL) for up to 15 min. After washing, the upper part of the membrane was carefully wiped off with a cotton-tipped swab. Cells migrated towards the lower side of the insert were observed by using an optical microscope (Eclipse TS100, Nikon, Japan). For cell quantification, migrated cells were lysed with 5 % oxalic acid solution and the absorbance was measured at 590 nm by using a microplate reader.

2.4.3. Scratch wound healing assay

To evaluate the effect of the different components of aerogels on cell migration, a scratch wound healing assay was performed [21]. The conditioned medium was collected by soaking the aerogels (10 mm × 10 mm; thickness, 0.30–0.35 mm) in 5 mL of low-serum (1 % FBS-supplemented medium) for up to 24 h. The HUVECs (4×10^4 cells per well) were seeded into a 24-well cell culture plate and cultured for up to 24 h to afford a confluent cell monolayer. Thereafter, a scratch of approximately 160 μm was created on the confluent cell monolayer by a 200 μL pipette tip and scratched cells were gently washed away with the PBS two times. Thereafter, each group received 2-mL of low-serum conditioned medium and was incubated for up to 24 h. Images of the migrated cells were collected at 0 and 24 h of culture by using an optical microscope (Eclipse TS100, Nikon, Japan), and quantitatively analyzed by using Image J (NIH, v1.8.0, USA) to determine the initial scratch area (C_0) and unhealed scratch area (C_1). The migration ratio was determined by Eq. (3):

$$\text{Migration ratio} = \left(\frac{C_0 - C_1}{C_0} \right) \times 100\% \tag{3}$$

where C_0 and C_1 represent initial scratch area and unhealed scratch area, respectively.

2.4.4. Alkaline Phosphatase Activity (ALP) and Alizarin Red S (ARS) Staining

For ALP activity, MC-3T3 and rBMSCs were seeded at a density of 2 × 10^4 cell/well into a 48-well cell culture plate and cultured for 12 h. Thereafter, the culture medium was replaced with the osteo-inductive medium (supplemented with 50 μg/mL ascorbic acid, 10 mM β-glycerophosphate and 10^{-8} M dexamethasone) and an equal volume of the extract solution was added. At day 14, cells were washed with the PBS two times and lysed by the cell lysate. The cell suspension was centrifuged at 10,000 rpm for 5 min and the supernatant was collected. The ALP activity was assessed using an Alkaline Phosphatase Assay Kit (P0321, Beyotime Biotechnology, Shanghai, China) according to the manufacturer's instructions. The amount of total protein in the supernatant was determined by a BCA protein detection kit (P0012S, Beyotime Biotech, Shanghai, China). The ALP activity was expressed with respect to the total protein content at day 14.

At day 14, ALP activity as well as ARS staining was performed following the manufacturer's instructions. The stained samples were photographed with the camera (Canon, EOS M200, Tokyo, Japan) while mineralized nodules were imaged by light microscope (TS100, Nikon, Tokyo, Japan). For the quantitative analysis of ARS staining, 1 mL of 10 % acetic acid was added to the stained cells and incubated at r.t. for 12 h. Then, the mixed solution was extracted and centrifuged at 13,000 rpm for 15 min. The absorbance was measured at 405 nm with a microplate reader (Thermo Fisher Multiskan FC, Thermo Fisher Scientific, Waltham, MA, USA).

2.4.5. Blood clotting assay

For blood clotting assay, samples were cut into circular shapes (φ, 8 mm; thickness, 3 mm) and pre-warmed at 37 °C for 30 min. About 100 μL of whole blood (containing 10 % sodium citrate) was dropped onto the surface of scaffolds; then, ca. 10 mL of DI water was gently added to rinse the unbound blood and samples were incubated in a shaker at 37 °C and 50 rpm for 5 min to collect the free erythrocytes after 5 min. Recalcified whole-blood (100 μL) was dissolved in 10 mL DI water and was used as a negative group. The hemoglobin solution was used as a reference and the OD was measured at 540 nm. The blood clotting index (BCI) was calculated by Eq. (4):

$$\text{BCI} = \frac{(D_T - D_R)}{(D_P - D_R)} \times 100\% \tag{4}$$

where D_T, D_P, and D_R represent the absorbance of the sample, negative control group, and reference value, respectively.

2.4.6. Tube-formation assay of HUVECs

About 100 μL of Matrigel TM (356234, BD Matrigel, USA) was pre-cooled at 4 °C, added into a 48-well cell culture plate and incubated at 37 °C for up to 10 min. The conditioned medium was collected by soaking the aerogels (10 mm × 10 mm; thickness = 0.30–0.35 mm) into 5 mL of free-serum for up to 24 h. About 200 μL of the conditioned medium obtained using different types of composite aerogels (n = 4) was added into a 48-well cell culture plate containing Matrigel. About 3×10^4 cells/well were seeded into the cell culture plate and cultured for up to 4 h to observe capillary-like structures using a light microscope (TS100, Nikon, Tokyo, Japan). Angiogenic network parameters, including nodes were quantified using Image J (NIH, v1.8.0, USA).

2.4.7. Osteogenic genes and protein expression

The expression of osteogenic genes was assessed by quantitative real-time PCR (qRT-PCR). At day 14 after cell culture, rBMSCs were treated with TRIzol reagent (Beyotime, Shanghai, China, 15596018). The total RNA was harvested and reverse-transcribed using reverse transcriptase kit to obtain the complementary DNA (cDNA). QuantStudio 3 Real-Time PCR System was used to detect the expression of osteogenic-related genes, including collagen type I (Col I), ALP, runt-related transcription factor-2 (Runx2), and osteopontin (OPN). The parameters used for the qRT-PCR analysis were as follow: 2 min at 50 °C, 10 min at 95 °C, 40 cycles of 95 °C for 15 s, 60 °C for 60 s, and a melting curve from 60 to 95 °C. The sequences of the primers used for qRT-PCR are given in Supplementary Information.

The expressions of Col I, BMP-2 (bone morphogenetic protein-2), and OPN were determined by western blotting analysis. The rBMSCs were cultured along with the extract solution obtained from the scaffolds for up to day 7. The total protein was extracted and the protein concentration was determined using a BCA protein assay kit. The samples were separated through sodium dodecyl sulfate–polyacrylamide gel electrophoresis (SDS-PAGE) and transferred to polyvinylidene fluoride membranes. Moreover, signal intensities of the protein bands were quantified by using ImageJ software.

2.5. Animal experiment in vivo

Protocols for the animal experiments were approved by the Institutional Animal Care and Use Committee (IACUC) of the Army Military Medical University (Number, AMUWEC20235044).

2.5.1. Subcutaneous implantation of scaffolds

The preliminary biocompatibility of the aerogel scaffolds was performed in a subcutaneous implantation model in rats. After anesthesia, the skin of SD rats was shaved and sterilized with 70 % ethanol. The midline was incised and a pocket was created. Scaffolds (n = 3, φ = 10 mm, thickness = 1.5 mm) were transplanted into the subcutaneous space and the skin was closed by a 5–0 silk sutures. Scaffolds alongside adjacent tissues and main organs were explanted at day 21 post-operatively. The explants were fixed with 4 % paraformaldehyde (PFA), paraffin-embedded, and sectioned into 5 μm thick slices (Beijing Jiayuan Xingye Technology Co., Ltd, HS-3315, Beijing, China). The explants as well as retrieved organs were processed for histological analysis by using hematoxylin and eosin (H&E) and Masson's trichrome (MT) staining.

2.5.2. Hemostatic ability of scaffolds in vivo

For a rat tail-amputation model, SD rats (n = 18, weight, 130–200 g) were amputated from the tail and randomly divided into 6 groups to either receive gauze (control group, 2 layers, 3 cm × 3 cm) or GD-BF1, GD-BF2, and GD-BF3 scaffolds (φ = 10 mm; thickness = 0.35 mm). Rats were anesthetized using intravenous (IV) administration of pentobarbital sodium (20–60 mg/kg) and a surgical cutting tool was used to trim ca. 50 % of the tail. The tail was left in the air for ca. 5 s to ascertain the normal blood loss.

For a rabbit ear artery injury model, the New Zealand white rabbits (weight, 2 kg; age = 4 weeks) were randomly divided into 4 groups, and were anesthetized using intravenous (IV) administration of pentobarbital sodium (20–60 mg/kg). The ear skin was shaved and the surgical site was sterilized to expose the artery. About 50 % of the circumference of the artery on the outer side of the ear was transected carefully to initiate the bleeding, and samples were immediately applied onto the bleeding site using a slight pressure. Thereafter, gauze, GD-BF1, GD-BF2, and GD-BF3 samples were used to evaluate hemostasis time as well as blood loss for all groups in both models (n = 3).

2.5.3. Wound healing in vivo

The SD rats (n = 24, weight, 190–210 g, 6 weeks old) were randomly divided into 4 groups, including control, GD-BF1, GD-BF2, and GD-BF3. Rats were anesthetized and the skin was sterilized and shaved. Full-thickness excisional defects (φ = 10 mm) were created on the dorsal side of the rats. The GD-BF1, GD-BF2, and GD-BF3 scaffolds (n = 5) were implanted into the defect site and were replaced every 3 days. Untreated wounds were used as controls. The digital images of the wounds were captured at day 0 as well as at day 3, 7, 10, 14, and 17 post-operatively. The wound length and wound areas were analyzed by tracing the wound margins and quantified by using Image J (National Institutes of Health, v1.8.0, USA). The wound closure rate was expressed as a percentage area of the original wound area and calculated by Eq. (5):

$$\text{Wound closure rate} = \left(1 - \frac{E_t}{E_0}\right) \times 100\% \tag{5}$$

where E_0 and E_t represent the area of the wounds at day 0 and at designated time intervals, respectively.

At pre-determined time points, the wounds along with their surrounding tissues from different groups were harvested, rinsed in PBS, and fixed in 4 % PFA immediately for 24 h at RT. Then tissues were embedded in paraffin and sectioned into 5 μm slices. Sections were counter-stained with H&E and MT staining.

2.5.4. Bone regeneration in vivo

Scaffolds were next transplanted into the femoral cavernous bone defect model (φ, 5 mm; depth, 5 mm) in the both feet of the rabbit. The eight New Zealand white rabbits (2-month-old) were randomly divided into control (without scaffold) or experimental groups (n = 4; e.g., GD-BF1, GD-BF2, GD-BF3, etc.). To sacrifice the rabbits, a lethal dose of 60 mg/mL of pentobarbital sodium (Mebunat; Orion Pharma, Finland) was injected into the marginal ear vein. The obtained specimens were scanned by the micro-CT equipment to observe the bone repair. After micro-CT analysis, the samples were decalcified by soaking in the decalcifying solution for up to one month at 37 ℃. Then the samples were dehydrated in gradient alcohol, embedded in paraffin, and sectioned into 5 μm slices. The slices were treated with H&E and MT staining.

2.6. Statistical analysis

All data were collected from three independent samples and quantitative data was expressed as mean ± standard deviation (SD). The statistical analysis was performed by using one-way analysis of variance (ANOVA) followed by Tukey's multiple comparison test and the criteria for statistical significance were *p < 0.05, **p < 0.01, ***p < 0.001.

3. Results

3.1. Structural analysis of aerogel scaffolds

The bioactive glass (BG) can furnish therapeutic ions to promote tissue repair process *in vitro* and *in vivo*. The composition of the BG can be varied to include the therapeutic ions of an interest. Despite the

potential advantages of the BG, it is used only for a handful of applications, such as a restorative material for the fracture healing [1]. On the other hand, electrospun membranes composed entirely of the BG may display poor mechanical properties alongside potential cytotoxicity risks [18]. To circumvent these limitations and offer an alternative solution for the fracture healing, we proposed the fabrication of short electrospun BG fibers as well as their assembly along with the Gel and DA (Fig. 1a–b). Appropriate proportions of short BG fibers (herein named as BGF) were blended along with Gel and DA (the resulting scaffolds were represented as GD-BGF$_x$, where x denotes the content of the BGF). The BG fibers were prepared from the calcination of electrospun PVP-BG fibers (Fig. 2).

Morphological analysis by SEM microscopy revealed smooth and uniform surface morphology of both the PVP-BG fibers and BG fiber membranes without insignificant morphological differences and the lack of a bead-like morphology (Fig. 2a). Quantitative analysis by the ImageJ showed that the average fiber diameters were 0.48 ± 0.15 μm and 0.35 ± 0.11 μm for PVP-BG and BG fibers, respectively (Fig. 2e–2f). These results indicate an insignificant effect of the calcination process on the morphology of the fibers. On the other hand, the homogenized BG fiber displayed an average fiber length of 12.30 ± 8.18 μm, while average fiber distribution was in the range of 0–40 μm (Fig. 2b & g).

The BGF were blended along with the Gel and DA to afford different types of aerogel scaffolds, including GD-BF1, GD-BF2, and GD-BF3. Since scaffolds were crosslinked with the DA, they exhibited brown colour (Fig. S1, Supporting Information). Moreover, since the scaffolds were crosslinked in the aqueous media, the DA may have been polymerized into the polydopamine. The SEM microscopy showed the formation of an interconnected lamellar-like porous structure. With an increase in the content of the BGF, the scaffolds displayed a microporous structure along with large pores (Fig. S1, Supporting Information). The XPS analysis of GD-BF2 scaffolds displayed a higher content of silicon (Si), while a lower content of calcium (Ca). The percentages of Si, Ca, and P were found to be 26.81 %, 1.96 %, and 3.19 %, respectively (Fig. 2h). The EDS mapping of the fibers further revealed a uniform distribution of Si, Ca, and P. Elemental percentage of Si, Ca, and P was found to be increased with an increase in the content of the BGF. These results show the successful synthesis of BGF as well as its dispersion in
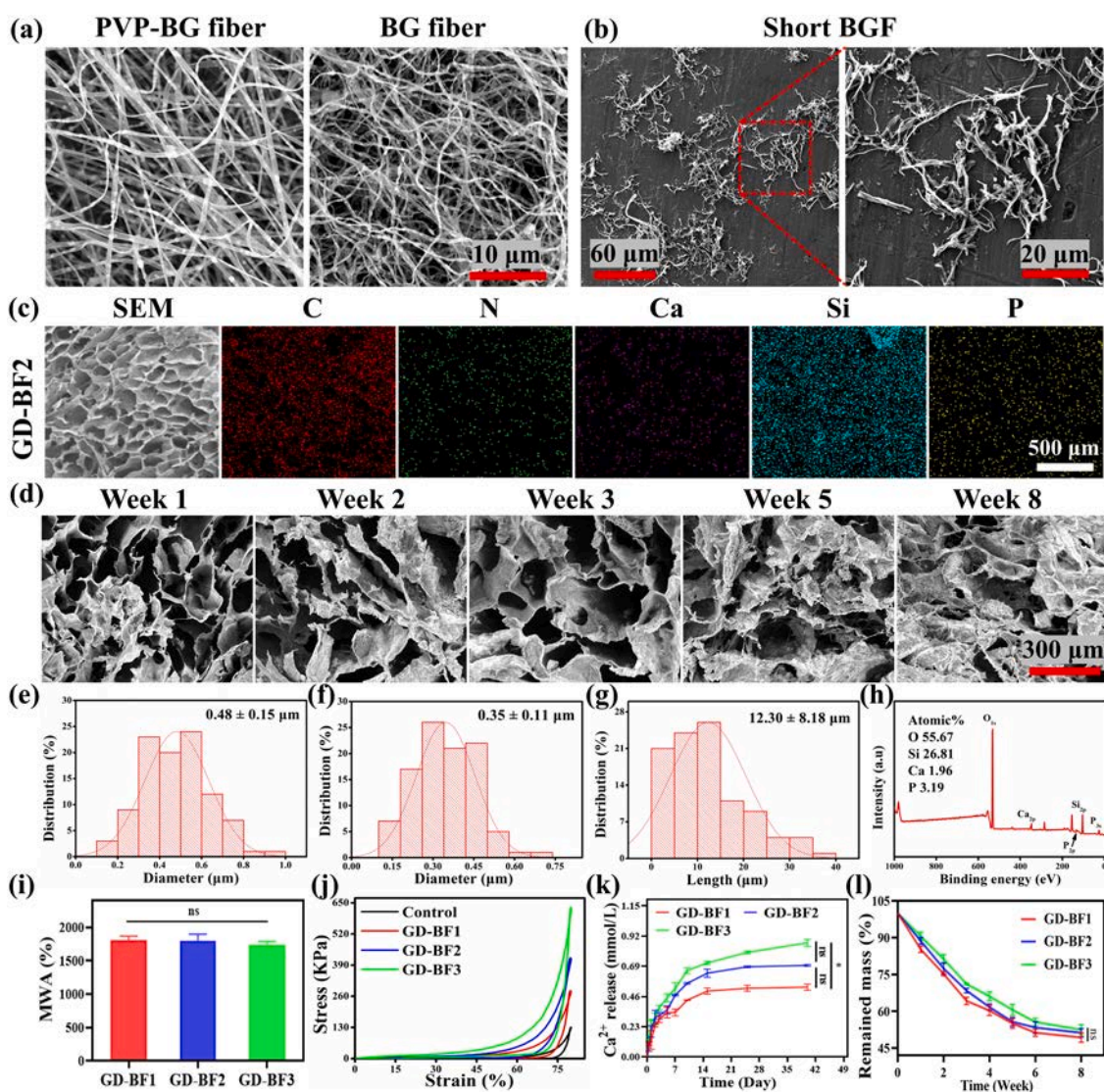

Fig. 2. Physico-chemical characterization of scaffolds. (a) SEM micrographs of PVP-BG and BG fiber membranes. (b) SEM micrographs of the BGF. The right panel in the Fig. 2b is an enlarged picture of the inset in the left panel in Fig. 2b. (c) SEM photomicrographs and EDX analysis of the GD-BF2 scaffold. (d) *In vitro* degradation of GD-BF2 scaffolds for up to 8 weeks. (e–f) Distribution of average fiber diameter of the PVP-BG and BG fibers. (g) Distribution of fiber length of the BGF. (h) XPS spectra of BGF. (i) The maximum water absorption (MWA) of scaffolds. (j) Representative compressive stress–strain curves of GD-BF1, GD-BF2, and GD-BF3 scaffolds. (k) Cumulative release of Ca^{2+} from the scaffolds. (l) Mass remained at different time points after *in vitro* degradation. $*p < 0.05$, $**p < 0.01$, and $***p < 0.001$.

the aerogels (Fig. 2c and Fig. S2, Supporting Information).

The porous morphology of scaffolds may help increase the water uptake. The values for the maximum water uptake (MWA) were 1809.6 ± 58.8 %, 1799.2 ± 102.6 %, and 1743.8 ± 46.7 % for GD-BF1, GD-BF2, and GD-BF3 scaffolds, respectively (Fig. 2i). The aerogel scaffolds were next subjected to the compressive testing. The mechanical properties of scaffolds were generally increased with the incorporation of the DA as well as with an increase in the BGF content; the GD-BF1 displayed

superior deformation recovery performance in the wet state (Fig. 2j, and Fig. S3, Supporting Information). As compared with the control group (G-BF1), the GD-BF1, which contained the DA manifested less fragmentation during the shock treatment, which is indicative of the good structural stability of the scaffolds (Fig. S4, Supporting Information). The cumulative release of calcium ions (Ca^{2+}) was increased with an increase in the BGF content and the values were found to be 0.53 ± 0.02, 0.70 ± 0.01, and 0.87 ± 0.03 mmol/L for GD-BF1, GD-BF2, and GD-BF3
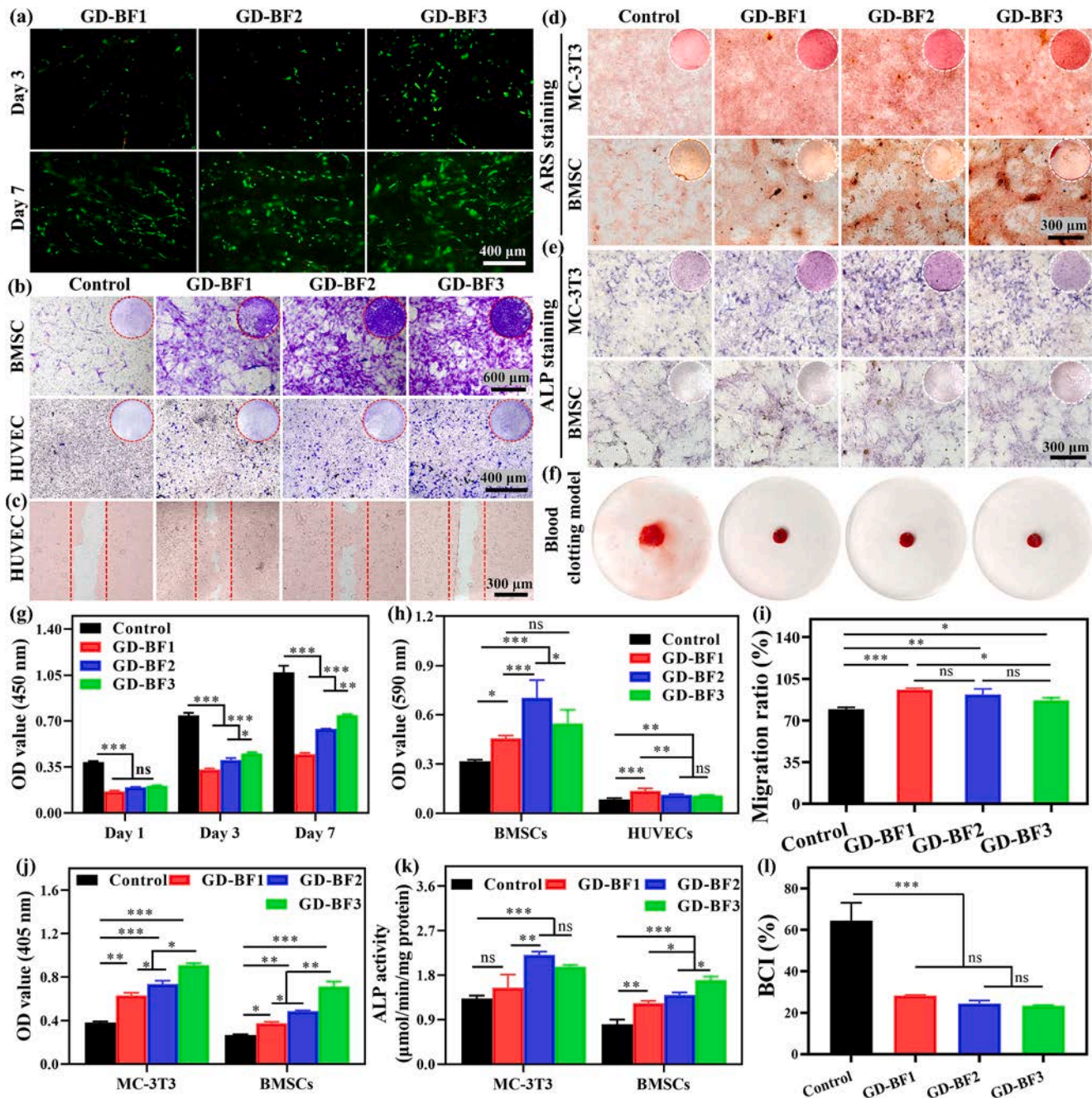
Fig. 3. (a) Cytocompatibility of scaffolds using rBMSCs. Cells were seeded on scaffolds and live/dead staining was performed at day 3 and 7. Scale bar, 400 μm. (b) Migration of rBMSCs and HUVECs evaluated by a Transwell migration assay. Scale bars, 400 μm and 600 μm. (c) Migration of HUVECs in a scratch wound healing assay *in vitro* at 24 h. Scale bar, 300 μm. (d) Alizarin Red S (ARS) staining of MC-3T3 and rBMSCs cultured along with the conditioned medium obtained from the different types of scaffolds at day 14. Scale bar, 300 μm. (e) Representative digital and microscopic images showing the ALP staining of MC-3T3 and rBMSCs cultured along with the conditioned medium obtained from the different types of scaffolds at day 14. Scale bar, 300 μm. (f) Digital photographs of BCI assay. (g) Quantitative analysis of the proliferation of rBMSCs on scaffolds using CCK-8 assay. (h) The OD values of the rBMSCs and HUVECs migrated in a Transwell migration assay *in vitro*. (i) Migration ratio of HUVECs in a scratch wound healing assay. Quantitative analysis of ARS staining (j) and ALP activity (k) of MC-3T3 and rBMSCs at day 14. (l) The BCI assay. *$p < 0.05$, **$p < 0.01$, and ***$p < 0.001$. (For interpretation of the references to colour in this figure legend, the reader is referred to the web version of this article.)

scaffolds, respectively (Fig. 2k). Meanwhile, the ICP analysis showed that the cumulative release value of silicon ions (Si^{4+}) and phosphate ions (PO_4^{3-}) were 2893.33 ± 36.96 ppm and 532.67 ± 29.37 ppm, respectively, at day 30, which is indicative of the sustained release of therapeutic ions from composite aerogels (Fig. S5, Supporting Information).

The degradation of scaffolds was discerned *in vitro*; all groups displayed considerable degradation over time, especially, during the first three weeks. The residual weight of the scaffolds was found to be 49.3 ± 2.0 %, 51.1 ± 1.7 %, and 52.4 ± 2.10 % for GD-BF1, GD-BF2, and GD-BF3 scaffolds, respectively, after 8 weeks (Fig. 2l). The rapid degradation of the scaffolds in the first 5 to 10 days may be ascribed to the degradation of the Gel. The SEM microscopy revealed the microporous structure of scaffolds; the scaffolds were gradually collapsed due to the swelling effect of the Gel (Fig. S6, Supporting Information). Nevertheless, the scaffold exhibited a stable structure both in the dry and wet states, which may be attributed to the DA-mediated crosslinking (Fig. S7a–7b, Supporting Information). The scaffolds can maintain their surface morphology even after degradation *in vitro*.

3.2. Biocompatibility and biofunctions of aerogel scaffolds

3.2.1. Biocompatibility of aerogel scaffolds

Biocompatibility, including hemocompatibility and cytocompatibility are important indicators for the successful applications of scaffolds for biomedical applications and were therefore studied *in vitro* (Fig. 3) [11]. Hemolysis assay revealed negligible hemolytic index of all groups. The hemolytic index was below 2 % in all groups, which is well-below the international standard of 5 % of hemolytic index (Fig. S8, Supporting Information). Live/dead staining manifested good viability of rBMSCs, thereby showing that the scaffolds were cytocompatible (Fig. 3a). The CCK-8 assay further showed continuous cell proliferation for up to 7 days (Fig. 3g). Cell proliferation was also slightly increased with an increase in the BGF content in the aerogel scaffolds, which is further indicative of the cytocompatibility of the BGF.

3.2.2. Biofunctions of scaffolds in vitro

The chemotaxis of rBMSCs and HUVECs was investigated using scratch wound healing assay and a Transwell migration assay. Aerogel scaffolds containing BGF induced considerable migration of both cell types as compared to the control group (Fig. 3b). The quantitative analysis was carried out by measuring the OD values of the cells migrated towards the lower side of the inserts. The scaffolds containing the BGF exhibited significantly higher OD values for rBMSCs than that of the control group (control, 0.32 ± 0.01; GD-BF, 0.46 ± 0.02; GD-BF2, 0.70 ± 0.11; and GD-BF3, 0.55 ± 0.08) (Fig. 3h). Scratch wound healing assay also manifested significant migration of HUVECs in the aerogel scaffolds containing the BGF as compared to their counterparts devoid of the BGF (control, 79.3 ± 1.7 %; GD-BF1, 96.1 ± 0.8 %; GD-BF2, 91.8 ± 4.8 %; and GD-BF3, 87.0 ± 2.2 %) (Fig. 3c & i). From these data, it can be inferred that while the BGF can promote the migration of HUVECs, its higher content may not exert a chemotactic effect. Generally, BGF had a significant role in promoting cell migration, which may also help improve cellular infiltration for tissue repair *in vivo* [10].

Since BGF may also promote osteogenesis as well as biomineralization, MC-3T3 and rBMSCs were co-cultured along with the conditioned medium obtained from the scaffolds followed by the cell staining with ARS and ALP. The incorporation of BGF manifested an obvious effect on the biomineralization of scaffolds than that of the control groups in both the MC-3T3 and rBMSCs culture conditions; the mineralization was further increased with an increase in the BGF content in the scaffolds (Fig. 3d). Quantitative analysis of the ARS revealed the significant deposition of mineral components alongside the deposition of the mineral matrix both by the MC-3T3 and rBMSCs (Fig. 3j). For ALP activity staining assay, BGF groups containing MC-3T3 and rBMSCs showed an intense purple colour at day 14, which is indicative of the good

biomineralization of the BGF containing groups over the control groups (Fig. 3e). Quantitative analysis of ALP staining further exhibited significantly higher ALP activity in BGF containing scaffolds than that of the control groups (Fig. 3k).

To probe whether the incorporation of the BGF can promote the hemostatic properties of scaffolds, hemolysis assay was performed using dynamic whole-blood clotting model *in vitro*. Aerogel scaffolds loaded with the BGF showed numerous residual blood clots as compared to the control group (Fig. 3f). The GD-BF groups also showed remarkably lower BCI values than that of the control group (Fig. 3l; control, 64.4 ± 8.7 %; GD-BF1, 28.2 ± 0.3 %; GD-BF2, 24.4 ± 1.6 %; GD-BF3, 23.3 ± 0.4 %).

To discern the angiogenic ability of the different types of scaffolds, the tube-formation assay was performed (Fig. 4). The obtained results are summarized in Fig. 4a. The GD-BF1, GD-BF2, and GD-BF3 groups displayed more number of nodes than that of control groups. The number of nodes were found to be 9.3 ± 1.7, 23.8 ± 5., 38.0 ± 6.3, and 20.3 ± 3.5 per HPF for control, GD-BF1, GD-BF2, and GD-BF3 groups, respectively (Fig. 4b).

The BG has also been shown to stimulate the production of osteogenic proteins as well as promote the osteogenic differentiation of cells. The osteogenic potential of the scaffolds was probed by performing RT-qPCR and western blotting analysis (Fig. 4). The scaffolds containing BGF expressed significantly higher levels of ALP, Runx2, and OPN than that of the control group (Fig. 4a–d). Western blot analysis further revealed significant production of osteogenic proteins, including Col I, BMP-2, and OPN as compared to the control group (Fig. 4e–f). These data showed an advantageous effect of the BGF to promote the osteogenic differentiation of rBMSCs, which may also have potential benefits for the biomineralization and osteogenesis of scaffolds *in vivo*.

3.3. Evaluation of scaffolds in vivo

3.3.1. Biocompatibility of aerogel scaffolds in a subcutaneous model

The preliminary biocompatibility of scaffolds was assessed in a subcutaneous implantation model in rats (Fig. 5). Histological analysis by the H&E staining revealed extensive host cell infiltration into the implanted scaffolds (Fig. 5b). Meanwhile, the extent of the residual scaffold was increased with an increase in the BGF content. The MT staining showed successful regeneration of collagen in the implanted scaffolds; the arrows point toward the regenerated collagen in the implanted scaffolds (Fig. 5c). For safety assessment, main organs, such as heart, liver, spleen, lung, and kidney of the animals receiving the transplants were stained with H&E. The implants did not induce an obvious toxicity to the most of the organs (Fig. 5d). These results showed that the aerogel scaffolds can be remodeled *in vivo* and the host cells can be accumulated along with regeneration of ECM components.

3.3.2. Hemostatic properties in vivo

The BGF contains therapeutic ions, such as calcium ions (Ca^{2+}) and silicon ions (Si^{4+}), which may promote blood coagulation [11]. Consequently, *in situ* hemostatic properties of scaffolds were discerned in a rat tail-amputation model and a rabbit ear artery injury model (Fig. 6a). Blood loss and hemostatic time were examined. The BGF groups, including GD-BF1, GD-BF2, and GD-BF3 exhibited significant hemostatic effect and manifested only a marginal blood loss in both of the models (Fig. 6b–c). Moreover, values for the blood loss and hemostatic time were also significantly less in the BGF containing groups than that of the control groups (Fig. 6d–e; rat tail amputation model: blood loss: control = 75.5 ± 8.7 mg, GD-BF1 = 38.2 ± 3.9 mg, GD-BF2 = 26.6 ± 2.1 mg, and GD-BF3 = 22.1 ± 1.2 mg; hemostasis time, control = 43.8 ± 1.5 s, GD-BF1 = 27.3 ± 1.3 s, GD-BF2 = 19.8 ± 1.5 s, and GD-BF3 = 16.8 ± 1.3 s). Similar results were obtained in a rabbit ear artery injury model (Fig. 6f–g; blood loss: control = 137.1 ± 8.1 mg, GD-BF1 = 54.7 ± 4.8 mg, GD-BF2 = 37.0 ± 3.6 mg, and GD-BF3 = 34.2 ± 1.7 mg; hemostasis time: control = 48.8 ± 3.0 s, GD-BF1 = 26.0 ± 2.5 s, GD-BF2 = 20.3 ± 1.3 s, and GD-BF3 = 20.5 ± 1.3 s).
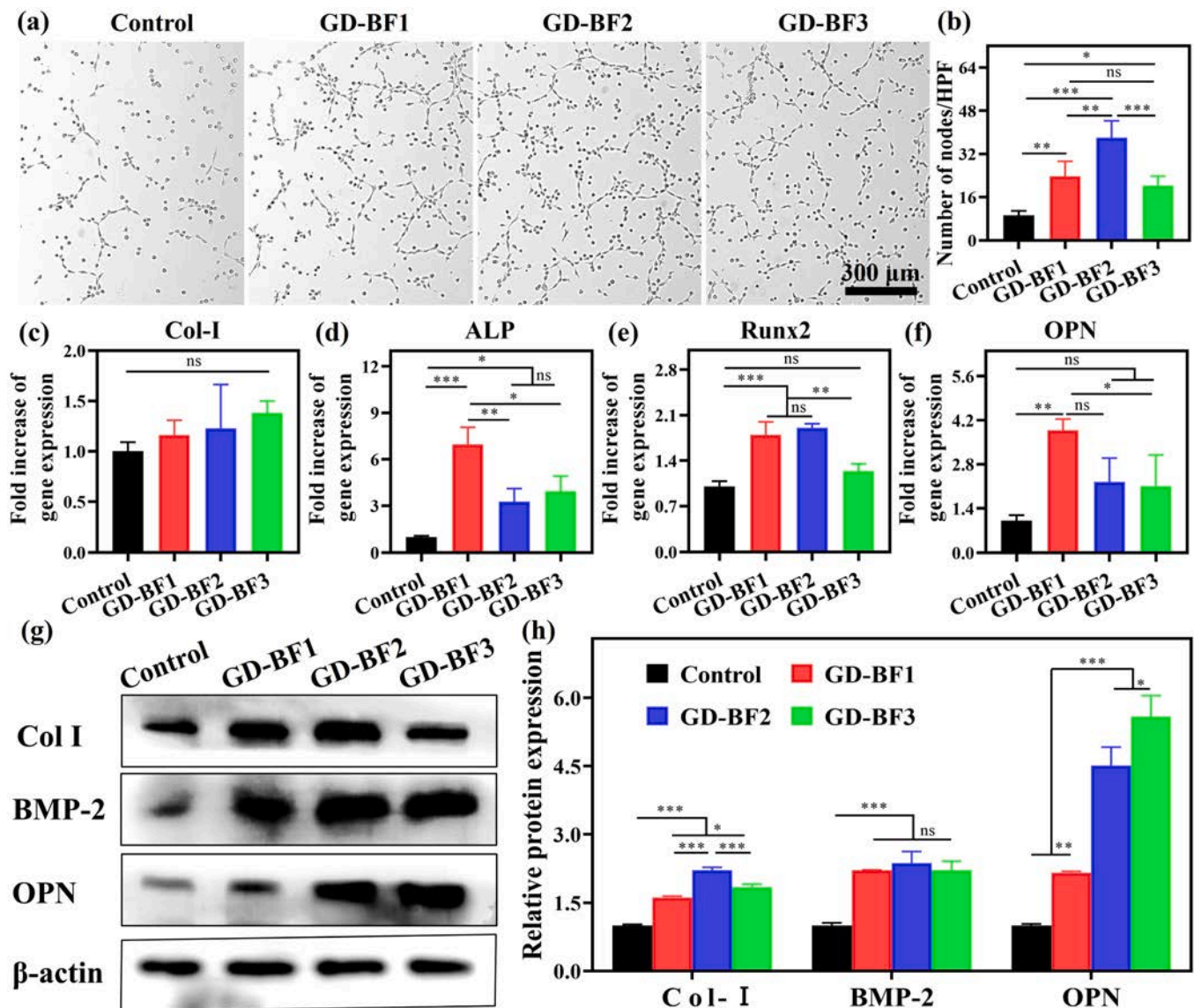
Fig. 4. The tube-formation assay of HUVECs and osteogenic differentiation of rBMSCs cultured along with the conditioned medium obtained from different types of scaffolds. The tubule-like network formation of HUVECs (a) and the quantitative analysis of number of nodes (b). Scale bar, 300 μm. The expression of different types of osteogenic genes, including Col I (c), ALP (d), Runx2 (e), and OPN (f) as evaluated by RT-qPCR at day 7. (g) Representative photographs collected after western blotting analysis. (h) Quantitative analysis of the expression of Col I, BMP-2, and OPN at day 14. $*p < 0.05$, $**p < 0.01$, and $***p < 0.001$.

3.3.3. Wound healing in vivo

Since aerogel scaffolds induced the migration of HUVECs and rBMSCs *in vitro* as well as recruited host cells *in vivo*, the bioactivity of the scaffolds was further assessed in a full-thickness excisional defect model in rats (Fig. 7a). Wounds in all groups manifested gradual healing and only a minute residual wound area was left by the day 17 (Fig. 7b). It is worth to note that the newly-generated skin surface of the wound was covered by the large numbers of hairs. In contrast, the wounds treated with the control group (gauze) manifested poor wound healing than that of their counterparts treated with the BGF containing scaffolds (Fig. 7d–7e). H&E staining of the explants revealed unhealed skin defects as well as only partially regenerated epithelium in the control group by the day 7. On the other hand, all groups containing BGF had achieved almost complete wound healing by the day 17 (Fig. 7c and Fig. S9, Supporting Information). Wounds treated with the GD-BF1, GD-BF2, and GD-BF3 aerogels showed significantly more thickness of the granulation tissues as compared to the control group (Fig. 7f; granulation tissue thickness: GD-BF1 = 1.65 ± 0.18 μm, GD-BF2 = 1.76 ± 0.11 μm, GD-BF3 = 1.88 ± 0.14 μm *vs.* control = 1.34 ± 0.09 μm).

The BGF groups also showed appreciably less scar length than that of the control groups. The values for the scar length were 2.16 ± 0.25 μm, 0.87 ± 0.15 μm, 0.92 ± 0.19 μm, 2.89 ± 0.31 μm for GD-BF1, GD-BF2, GD-BF3, and control groups, respectively (Fig. 7g). The MT staining showed deposition and maturation of collagen within the healed wounds as well as the formation of organized fibroblasts encased in the ECM, which were further increased with an increase in the implantation time (Fig. 7c and Fig. S9, Supporting Information). The skin appendages formation (e.g., hair follicles, glands, etc.) were gradually matured; the number and the distribution of skin glands was similar to that of the normal skin, especially in the GD-BF1 and GD-BF2 groups (Fig. 7h and Fig. S10, Supporting Information).

3.3.4. Bone regeneration in vivo

Scaffolds were next transplanted into a femoral defect model in rabbits and were evaluated for up to 6 weeks (Fig. 8). The normal femoral head exhibited a relatively symmetrical structure on the both sides and a relatively smooth surface (Fig. 8a). The control group (scaffolds lacking BGF) showed bone hyperplasia after 6 weeks, which
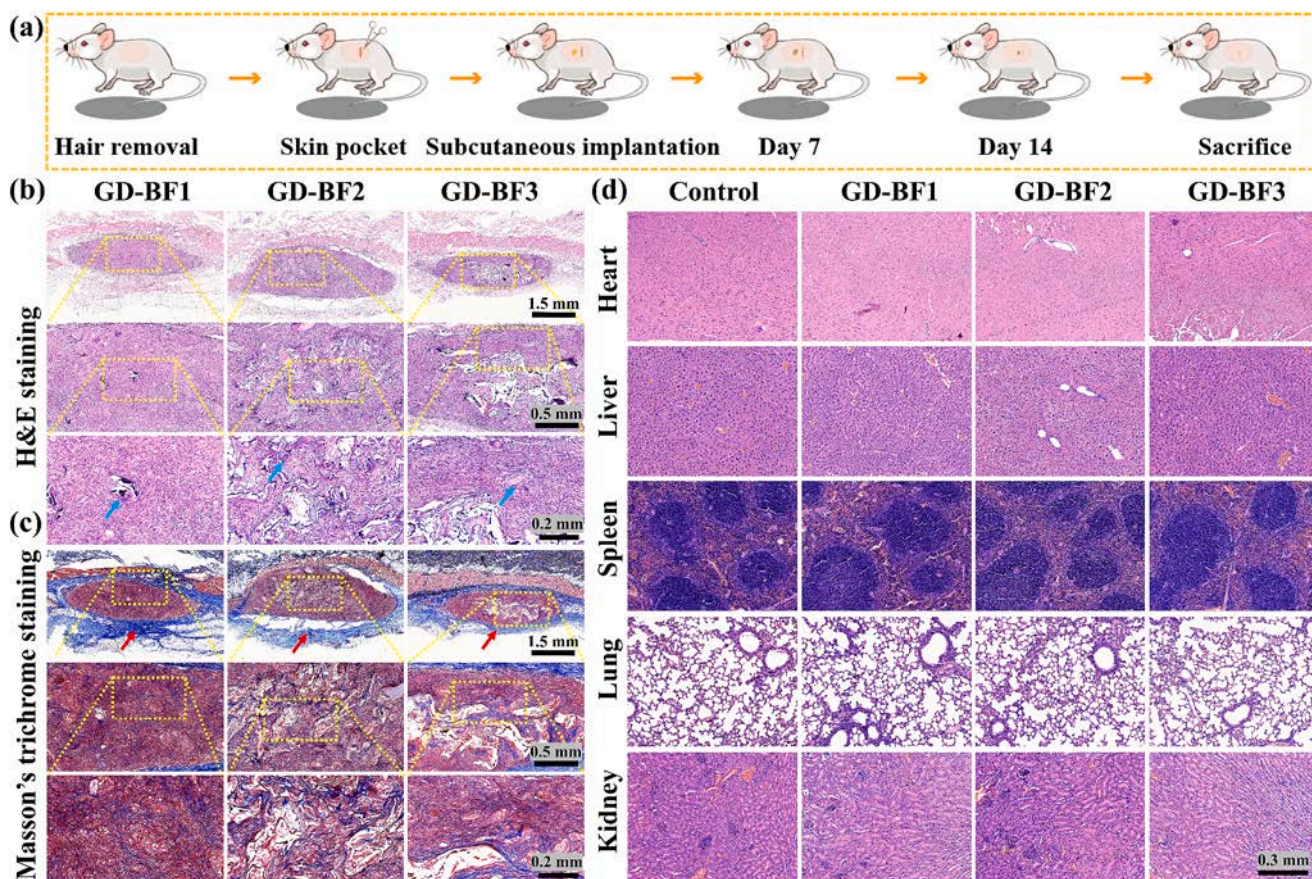
Fig. 5. Preliminary biocompatibility of aerogel scaffolds in a subcutaneous implantation model *in vivo*. (a) Schematic representation of the implantation of scaffolds in rats for up to 21 days. (b) H&E and (c) MT staining of explanted scaffolds. (d) H&E staining of main organs, including heart, liver, spleen, lung, and kidney collected from animals receiving implants at day 21 post-operatively. Blue arrows point toward residual scaffold, while red arrows point toward regenerated collagen. (For interpretation of the references to colour in this figure legend, the reader is referred to the web version of this article.)

led to the significant enlargement of the femoral head. The GD-BF1, GD-BF2, and GD-BF3 scaffolds suppressed bone hyperplasia after femur damage (Fig. 8a). The 3D reconstructed CT images further showed the formation of ectopic hyperplasia of bone in the control group, while negligible ectopic hyperplasia in the BGF containing scaffolds (Fig. 8b). It is worth to notice that the GD-BF1, GD-BF2, and GD-BF3 scaffolds significantly induced biomineralization in the bone defects 6 weeks post-operatively.

Histological analysis by H&E staining showed that the BGF containing scaffolds underwent significant degradation alongside inducing appreciable bone formation in the defect site (Fig. 8c). In striking contrast, the control group lacked bone regeneration in the defect (Fig. 8c). The MT staining showed only a minute accumulation of collagen in the control group, while significant deposition of collagen in BGF groups (Fig. 8d). Taken together, these results indicate that the BGF scaffolds may not only inhibit bone hyperplasia, but they may also promote the mineralization of bone defects as well as induce the regeneration of collagen, thereby accelerating the reconstruction of bone tissue in bone defects.

4. Discussion

Electrospun fibers are widely used for numerous applications ranging from the electronics to the environmental remediation to the biotechnology. While the morphology of the fibers can be tailored by varying different types of electrospinning parameters, dense fibers pose an impediment for the potential utilization of electrospun scaffolds for tissue regeneration presumably due to poor cell infiltration and neo-

tissue formation as well as weak mechanical properties [22]. Especially, for the bone tissue repair, the scaffolds require appropriate mechanical properties for their successful implantation into the bone defects. We and other researchers have designed aerogel scaffolds, which may have potential biotechnological applications, thanks to their morphological similarity to the osteochondral tissues. Nevertheless, aerogel scaffolds require bioactive components to harness their full potential for bone tissue repair. Therefore, additional bioactive cues which can actively promote tissue repair through multiple effects may hold considerable significance for the potential applicability of aerogel scaffolds.

The bioactive glasses (BGs) with varying elemental compositions are shown to simultaneously promote angiogenesis and osteogenesis for different types of applications, such as wound healing, bone regeneration, and so on. Despite the unique advantages of the BGs, the poor mechanical properties and inherent brittleness may compromise their application prospects. We widened the application prospect of BGs by converting them into electrospun fibers. Moreover, we exploited the DA to promote the thermal crosslinking of the scaffolds (Fig. 1b). The crosslinking among the carboxylic groups (–COOH) of the Gel and the amino (–NH$_2$) groups of the DA may improve the structural stability of aerogel scaffolds (Fig. 1b). The improved structural stability led to the lower water solubility of aerogels [1,23]. The DA may undergo self-polymerization, thereby affording versatile reactivity under thermal treatment [24,25]. The adhesive moieties of the DA, including catechol may help functionalize the biomaterials, which may also be beneficial to tailor cell-materials interactions [26]. The DA receptor and DA signaling pathway can also affect the osteogenic activity of cells [27]. In addition
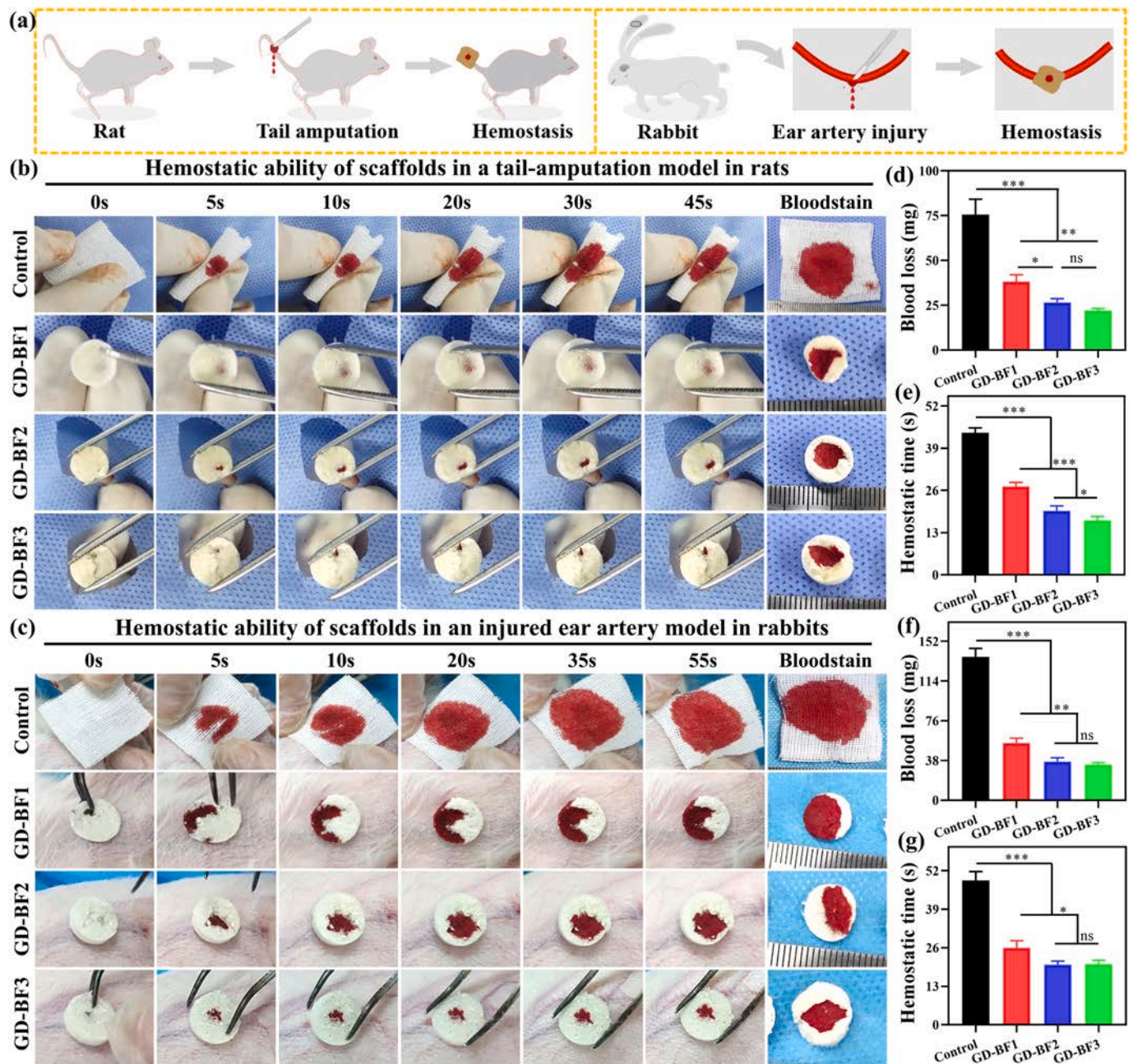
Fig. 6. Hemostatic performance of scaffolds *in vivo*. Schematic representation of a rat tail-amputation model and a rabbit ear artery injury model for hemostatic assay (a). Representative photographs showing implantation of scaffolds in a rat tail amputation model (b) and an ear artery injury model in rabbits (c). Quantitative analysis of blood loss (d, f) and hemostasis time (e, g). *$p < 0.05$, **$p < 0.01$, and ***$p < 0.001$.

to these potential benefits, the therapeutic ions released from the scaffolds may also be helpful for tissue repair. We indeed observed significant weight loss of scaffolds alongside considerable release of calcium ions (Ca^{2+}) and silicon ions (Si^{4+}) upon their incubation into the PBS for up to 5 weeks *in vitro* (Fig. 2k–l).

Microporous aerogels may further help absorb tissue exudate as well as improve blood coagulation alongside improving the diffusion of oxygen as well as the transport of nutrients. The aerogel scaffolds displayed microporous structure as well as exhibited improved mechanical properties This improvement in the mechanical properties may be ascribed to the incorporation of BGF as well as thermal crosslinking between Gel and DA.

The BGF may furnish therapeutic ions, such as calcium ions (Ca^{2+}) and silicon ions (Si^{4+}); these ions can promote cell growth as well as

increase the deposition of ECM components. The therapeutic ions may also promote the formation of skin appendages during wound healing as well as induce osteogenic differentiation and mineralization during bone repair [11,28]. Indeed, we observed significant increase in cell proliferation, osteogenic differentiation, and biomineralization *in vitro* (Fig. 3a, d–e). We also observed significantly higher expression levels of Col I, ALP, Runx2, and OPN in the BGF containing aerogel scaffolds than that of the groups devoid of the BGF (Fig. 3c–h). The scaffolds containing the BGF scaffolds could also release phosphate ions (PO_4^{3-}), which are the potential mineralization resource (Fig. S5, Supporting Information). These phosphate ions could facilitate bone repair by promoting the deposition of calcium phosphate as well as stimulate osteogenesis to enhance the formation of new bone [29,30].

The *in vivo* implantation of scaffolds revealed host cell infiltration,
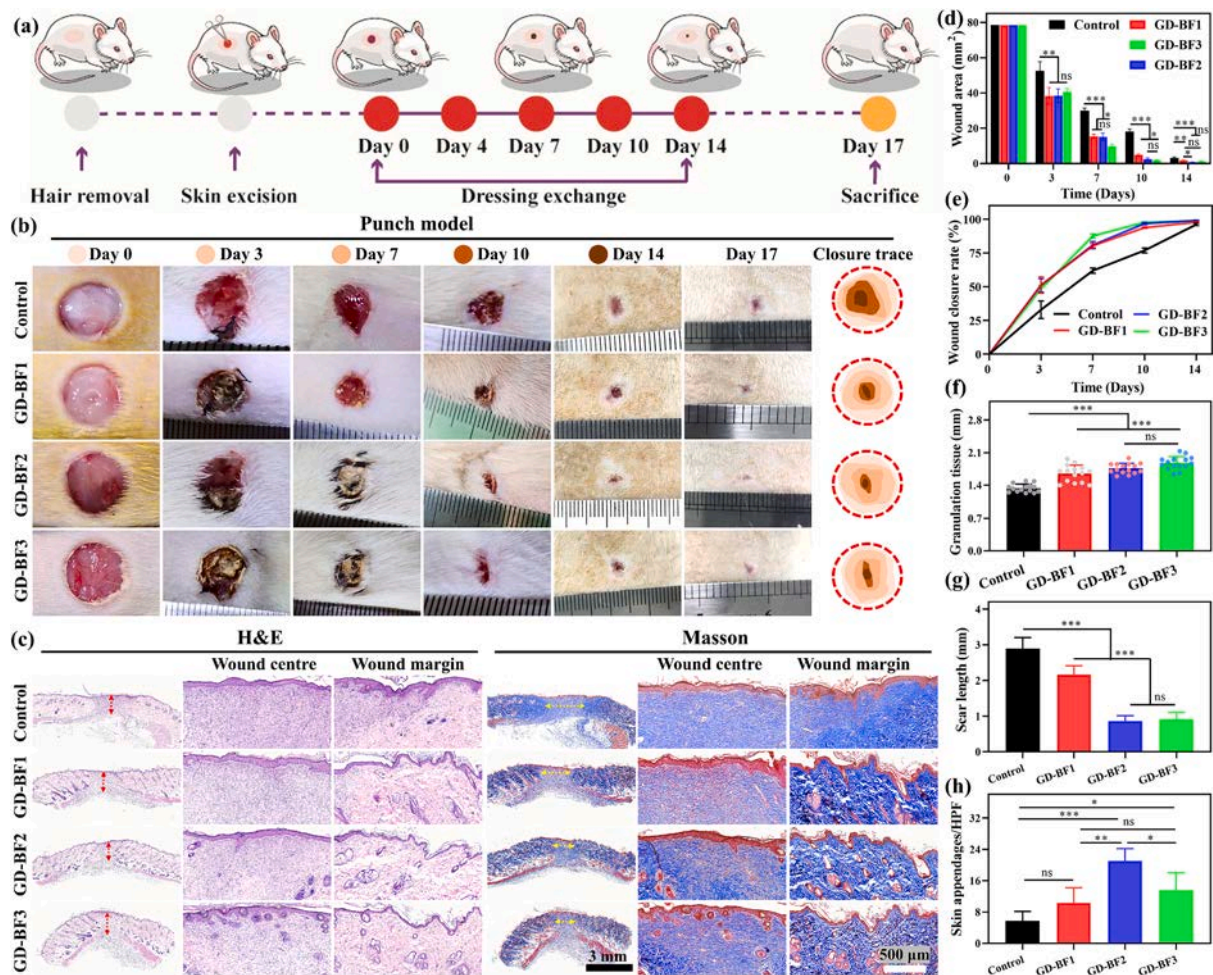
Fig. 7. Transplantation of scaffolds in a full-thickness excisional defect model in rats. The control group was treated with the gauze. The GD-BF1, GD-BF2, and GD-BF3 scaffolds were used as experimental groups. (a) Schematic diagram showing the different steps of the implantation of scaffolds, as well as the timeline for the replacement of new scaffolds and the collection of samples. (b) Representative images of wound area and closure trace of wounds for up to day 17. (c) The H&E staining and MT staining of explanted wound tissues at day 17. Scale bars, 3 mm and 0.3 μm. (d) Wound area at different time points normalized with respect to day 0. (e) Wound healing concomitantly increased for up to 17 days. (f) Thickness of granulation tissues, (g) scar length, and (h) number of skin appendages (hair follicles and glands) per high power field (HPF) by day 14. $*p < 0.05$, $**p < 0.01$, and $***p < 0.001$.

neo-tissue formation, and collagen deposition. Moreover, scaffolds were found to be biocompatible as they did not induce cytotoxicity to different types of organs *in vivo* [31]. Hemostasis is the first step in the wound healing process, which prevents blood loss before the initiation of complex mechanisms for cell proliferation, and tissue remodeling [32]. Since there are large number of blood vessels around the bone tissue, the timely hemostasis at the transplantation site may help reduce the blood leakage [33–35].

The *in situ* hemostatic ability of aerogel scaffolds was discerned in a rat tail-amputation model and a rabbit ear artery injury model. The scaffolds manifested significant hemostatic properties in both of the models in term of hemostatic time and blood loss. The good hemostatic ability of scaffolds may be ascribed to the activation of the intrinsic and extrinsic coagulation pathways as well as the formation of clots (Fig. 6b–c) [11,36]. Since the scaffolds can rapidly uptake the moisture as well as act as physical barriers, they can block the bleeding at the hemorrhage site. The scaffolds loaded with BGF may additionally release calcium ions (Ca^{2+}) and silicon ions (Si^{4+}), which may promote the phosphorylation of platelet protein by the protein kinase C (PKC), activate intrinsic and extrinsic coagulation pathways, and increase platelet activation and aggregation to stimulate the blood coagulation cascade. The aerogel scaffolds with sufficient porosity and pores may further improve the adhesion of RBCs as well as platelets to accelerate

blood coagulation [37,38]. The GD-BF1 and GD-BF2 showed good hemostatic effect with an increase in the BGF content (Fig. 6d–g).

To further validate the potential of the aerogel scaffolds for the soft tissue regeneration, a full-thickness excisional wound model was established in rats and scaffolds were transplanted at the injury site for up to 17 days. After treatment with the aerogel scaffolds, the wounds were rapidly filled with neo-tissues and were accompanied by the rapid re-epithelialization and regular collagen deposition. We also observed remarkably more numbers of hair follicles and sweat glands in GD-BF2 and GD-BF3 aerogels (Fig. 7c). The skin defects treated with GD-BF2 showed almost similar distribution of skin appendages to that of the normal skin, which is indicative of their potential to promote wound healing. The released therapeutic ions (Ca^{2+} and Si^{4+}) may promote the expression of vascular endothelial growth factor (VEGF) in HUVECs, thereby facilitating angiogenesis and vascular maturation [34,39]. Taken together, these results reveal the good potential of scaffolds for hemostasis and wound repair.

The aerogel scaffolds could promote bone formation by concurrently inducing osteogenesis and angiogenesis, thanks to the release of therapeutic ions (Si^{4+} and Ca^{2+}) [40,41]. The porous aerogel scaffolds could support the diffusion of oxygen as well as increase the transport of nutrients [42]. Indeed, we observed significant bone regeneration alongside minimal bone hyperplasia in the implanted scaffolds containing the
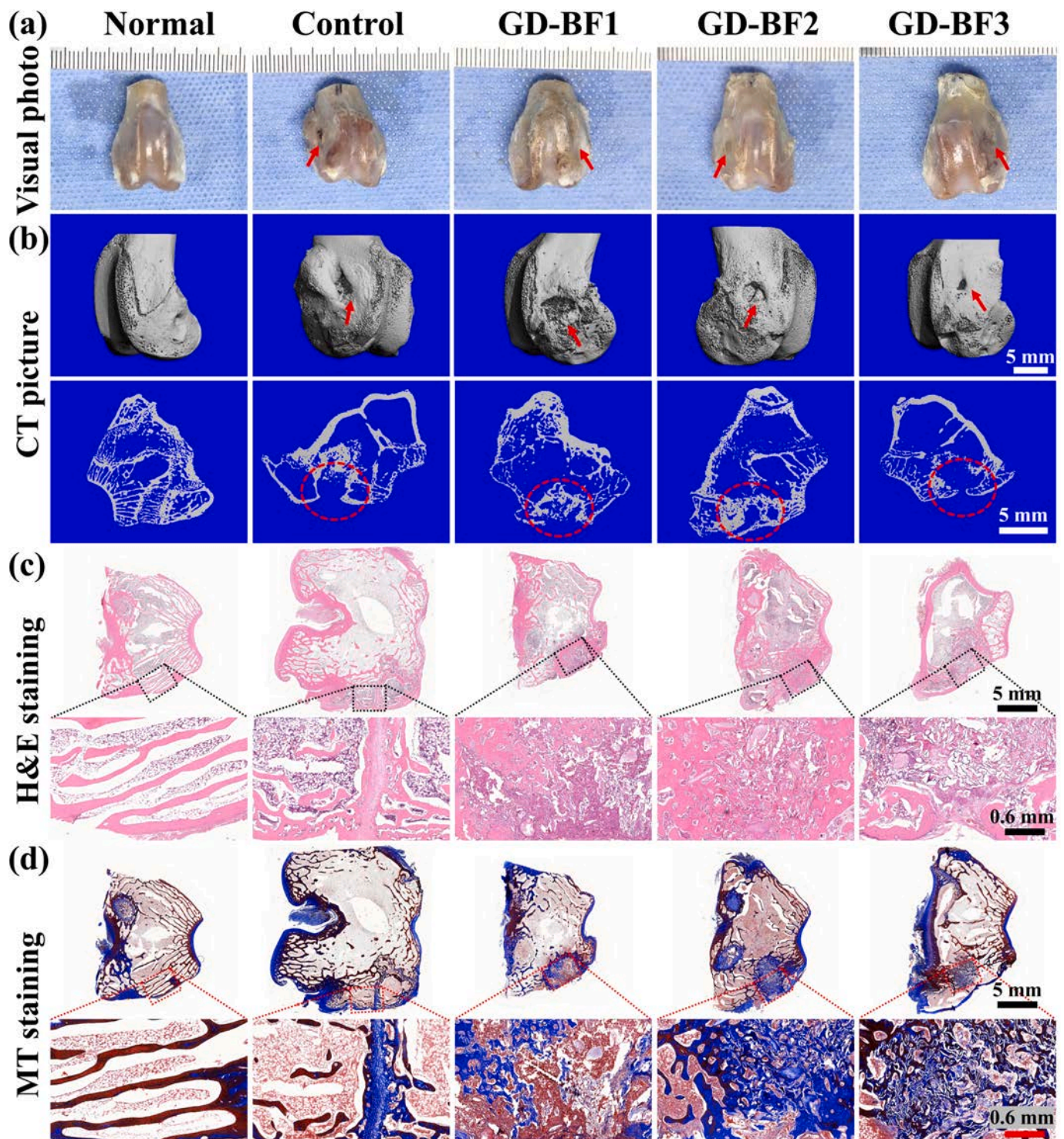
Fig. 8. Transplantation of aerogel scaffolds in a femoral defect model in rabbits for up to 6 weeks. (a) Digital photographs and (b) 3D reconstructed micro-CT images of femoral after 6 weeks. Scale bar, 5 mm. (c–d) Histological analysis of the normal bone and new bone formed at the fracture site 6 weeks post-operatively. H&E staining (c) and MT staining (d). Scale bars, 5 mm and 0.6 μm.

BGF than that of the control group in a femoral defect implantation model *in vivo* (Fig. 8a–b). The GD-BF2 induced significant mineralization and collagen deposition than that of the GD-BF1 and GD-BF3 groups. Collectively, we observed good hemostatic ability of scaffolds along with their potentials to induce skin and bone tissue repair. These aerogel scaffolds are worthy of future investigations with potential utilization for soft and hard tissue repair, which may increase hemostasis, wound healing and bone tissue regeneration. The GD-BF2 scaffolds manifested

good application prospect partly due to the presence of appropriate organic and inorganic components alongside suitable structural characteristics.

There are also various limitations in this study, which need to be carefully addressed to harness therapeutic benefits from these scaffolds. The GD-BF2 scaffolds displayed good therapeutic effect for bone and skin regeneration, thus we could design the scaffolds with the gradient structure, which may help discern their application prospect for

musculoskeletal tissue regeneration. Moreover, the DA was incorporated into the scaffolds to improve their structural stability. It is worthy to note that the DA can be polymerized into polydopamine during mixing in aqueous media via covalent oxidative polymerization and physical self-assembly pathways [43]. While, the detailed mechanism of the crosslinking of the composite aerogel using dopamine yet remains to be deciphered, the composite aerogels were appeared to be of the brown colour following the crosslinking [44–46]. It is anticipated that during the crosslinking process and the mixing in the aqueous media, the dopamine may have turned into polydopamine. Nevertheless, the available catechol moieties can participate in the crosslinking process with the other components of the aerogels.

5. Conclusion

In summary, we have successfully prepared BGF by electrospinning and calcination followed by their blending along with the DA and Gel to afford aerogel scaffolds. We deciphered structural and morphological properties of aerogel scaffold as well as carried out a series of *in vitro* experiments, which revealed substantial effect of the BGF-mediated therapeutic ions in leveraging multiple functionalities, such as rapid coagulation properties, improved chemotaxis, and osteogenic activity *in vitro*. The biocompatibility of aerogel scaffolds revealed infiltration of host cells as well as the formation of neo-tissues. The full thickness excisional wound model showed that the GD-BF2 scaffolds could improve wound re-epithelialization, collagen deposition and skin appendages formation. Similarly, the scaffolds containing the BGF exhibited good hemostatic ability in a rat tail-amputation model and a rabbit ear artery injury model. In addition, GD-BF2 scaffolds induced significant bone regeneration and deposition of the ECM components in a femoral defect model alongside minimal bone hyperplasia. Taken together, these aerogel scaffolds are worthy for future investigations and may also have potential applicability in soft and hard tissue repair.

CRediT authorship contribution statement

Zhengchao Yuan: Writing – original draft, Validation, Investigation, Conceptualization. **Lixiang Zhang:** Visualization, Software, Methodology, Conceptualization. **Muhammad Shafiq:** Validation, Methodology, Investigation. **Xinyi Wang:** Visualization, Supervision, Resources, Methodology, Funding acquisition. **Pengfei Cai:** Validation, Software, Methodology, Data curation. **Abdul Hafeez:** . **Yangfan Ding:** Visualization, Supervision, Project administration, Methodology, Conceptualization. **Zewen Wang:** Supervision, Project administration, Funding acquisition, Formal analysis. **Mohamed EL-Newehy:** Validation, Supervision, Methodology, Investigation. **Meera Moydeen Abdulhameed:** Writing – original draft, Validation, Supervision, Resources. **Lianyong Jiang:** Writing – review & editing, Resources, Funding acquisition, Data curation. **Xiumei Mo:** Writing – review & editing, Supervision, Project administration, Funding acquisition. **Yuan Xu:** Validation, Supervision, Software, Resources, Formal analysis.

Declaration of competing interest

The authors declare that they have no known competing financial interests or personal relationships that could have appeared to influence the work reported in this paper.

Data availability

The data that has been used is confidential.

Acknowledgements

Appendix A. Supplementary data

Supplementary data to this article can be found online at https://doi.org/10.1016/j.jcis.2024.06.098.

References

[1] M. Liu, M. Shafiq, B. Sun, J. Wu, W. Wang, M. EL-Newehy, H. EL-Hamshary, Y. Morsi, O. Ali, A.U.R. Khan, X. Mo, Composite superelastic aerogel scaffolds containing flexible SiO_2 nanofibers promote bone regeneration, Adv. Healthc. Mater. 11 (2022) 2200499.

[2] X. Wang, J. Xue, B. Ma, J.F. Wu, J. Chang, M. Gelinsky, C. Wu, Black bioceramics: combining regeneration with therapy, Adv. Mater. 32 (2020) 2005140..

[3] T. Kageyama, H. Akieda, Y. Sonoyama, K. Sato, H. Yoshikawa, H. Isono, M. Hirota, H. Kitajima, Y.S. Chun, S. Maruo, J. Fukuda, Bone beads enveloped with vascular endothelial cells for bone regenerative medicine, Acta Biomater. 165 (2022) 168–179.

[4] S. Gupta, I. Qayoom, P. Gupta, A. Gupta, P. Singh, S. Singh, A. Kumar, Exosome-functionalized, drug-laden bone substitute along with an antioxidant herbal membrane for bone and periosteum regeneration in bone sarcoma, ACS Appl. Mater. Interfaces. 15 (2023) 8824–8839.

[5] X. Zhang, Q. Li, L. Li, J. Ouyang, T. Wang, J. Chen, X. Hu, Y. Ao, D. Qin, L. Zhang, J. Xue, J. Cheng, W. Tao, Bioinspired mild photothermal effect-reinforced multifunctional fiber scaffolds promote bone regeneration, ACS Nano. 17 (2023) 6466–6479.

[6] P. Feng, P. Wu, C. Gao, Y. Yang, W. Guo, W. Yang, C. Shuai, A multimaterial scaffold with tunable properties: toward bone tissue repair, Adv. Sci. 5 (2018) 1700817.

[7] S. Lian, Z. Mu, Z. Yuan, M. Shafiq, X. Mo, W. Mu, Methacrylated gelatin and Platelet-Rich plasma based hydrogels promote regeneration of Critical-Sized bone defects, Regen. Biomater. 11 (2024) rbae022.

[8] C. Shuai, W. Yang, P. Feng, S. Peng, H. Pan, Accelerated degradation of HAP/PLLA bone scaffold by PGA blending facilitates bioactivity and osteoconductivity, Bioact. Mater. 6 (2021) 490–502.

[9] S. Tomar, R. Pandey, P. Surya, R. Verma, R. Mathur, G. Gangenahalli, S. Singh, Multifunctional, adhesive, and PDA-coated bioactive glass reinforced composite hydrogel for regenerative wound healing, ACS Biomater. Sci. Eng. 9 (2023) 1520–1540.

[10] X. Zhang, Y. Li, Z. Ma, D. He, H. Li, Modulating degradation of sodium alginate/bioglass hydrogel for improving tissue infiltration and promoting wound healing, Bioact. Mater. 6 (2021) 3692–3704.

[11] Z. Yuan, L. Zhang, S. Jiang, M. Shafiq, Y. Cai, Y. Chen, J. Song, X. Yu, H. Ijima, Y. Xu, X. Mo, Anti-inflammatory, antibacterial, and antioxidative bioactive glass-based nanofibrous dressing enables scarless wound healingSmart Materials in Medicine nano fibrous dressing enables scarless wound healing, Smart Mater. Med. 4 (2023) 407–426.

[12] S. Li, X. Wu, N. Bai, J. Ni, X. Liu, W. Mao, L. Jin, H. Xiang, H. Fu, Q. Shou, Fabricating oxidized cellulose sponge for hemorrhage control and wound healing, ACS Biomater. Sci. Eng. 9 (11) (2023) 6398–6408.

[13] X. Liu, B. Gaihre, L. Li, A. Rezaei, M. Tilton, B.D. Elder, L. Lu, Bioorthogonal "Click Chemistry" bone cement with bioinspired natural mimicking microstructures for bone repair, ACS Biomater. Sci. Eng. 9 (3) (2023) 1585–1597.

[14] T. Mehrabi, A.S. Mesgar, Z. Mohammadi, Bioactive glasses: a promising therapeutic ion release strategy for enhancing wound healing, ACS Biomater. Sci. Eng. 6 (10) (2020) 5399–5430.

[15] S. Li, Z. Li, J. Yang, Z. Ha, X. Zhou, C. He, Inhibition of sympathetic activation by delivering calcium channel blockers from a 3D printed scaffold to promote bone defect repair, Adv. Healthc. Mater. 11 (2022) 2200785.

[16] L. Ma, Y. Zhou, Z. Zhang, Y. Liu, D. Zhai, H. Zhuang, Q. Li, J. Yuye, C. Wu, J. Chang, Multifunctional bioactive Nd-Ca-Si glasses for fluorescence thermometry, photothermal therapy, and burn tissue repair, Sci. Adv. 6 (2020) eabb1311.

[17] S.D. Aker, S. Tamburaci, F. Tihminlioglu, Development of cissus quadrangularis-loaded poss-reinforced chitosan-based bilayer sponges for wound healing applications: drug release and in vitro bioactivity, ACS Omega. 8 (22) (2023) 19674–19691.

[18] X. Liu, X. He, D. Jin, S. Wu, H. Wang, M. Yin, A. Aldalbahi, M. El-Newehy, X. Mo, J. Wu, A biodegradable multifunctional nanofibrous membrane for periodontal tissue regeneration, Acta Biomater. 108 (2020) 207–222.

[19] W. Liu, D. Zhai, Z. Huan, C. Wu, J. Chang, Novel tricalcium silicate/magnesium phosphate composite bone cement having high compressive strength, in vitro bioactivity and cytocompatibility, Acta Biomater. 21 (2015) 217–227.

[20] Z. Yuan, Y. Zhao, M. Shafiq, J. Song, J. Hou, Y. Liang, X. Yu, Y. Chenm, F. Yu, M. EL-Newehy, H. EL-Hamshary, Y. Morsi, S. Jiang, H. Zheng, X. Mo, Multi - functional fibrous dressings for burn injury treatment with pain and swelling relief and scarless wound healing, Adv. Fiber Mater. 5 (2023) 1963–1985.

[21] Q. Zeng, Y. Han, H. Li, J. Chang, Design of a thermosensitive bioglass/agarose-alginate composite hydrogel for chronic wound healing, J. Mater. Chem. b. 3 (2015) 8856–8864.

[22] W. Chen, Y. Xu, Y. Liu, Z. Wang, Y. Li, G. Jiang, X. Mo, G. Zhou, Three-dimensional printed electrospun fiber-based scaffold for cartilage regeneration, Mater. Des. 179 (2019) 107886.

[23] Z. Yuan, Y. Ren, M. Shafiq, Y. Chen, H. Tang, B. Li, M. EL-Newehy, H. EL-Hamshary, Y. Morsi, H. Zheng, X. Mo, Converging 3D printing and electrospinning: effect of poly(L-lactide)/gelatin based short nanofibers aerogels on tracheal regeneration, Macromol. Biosci. (2021) 2100342.

[24] Y. Gao, J. Chen, X. Han, Y. Pan, P. Wang, T. Wang, T. Lu, A universal strategy for tough adhesion of wet soft material, Adv. Funct. Mater. 30 (2020) 2003207.

[25] K. Liu, X. Dong, Y. Wang, X. Wu, H. Dai, Dopamine-modified chitosan hydrogel for spinal cord injury, Carbohydr. Polym. 298 (2022) 120047.

[26] R. Pahuja, K. Seth, A. Shukla, R.K. Shukla, P. Bhatnagar, L.K.S. Chauhan, P. N. Saxena, J. Arun, B.P. Chaudhari, D.K. Patel, S.P. Singh, R. Shukla, V.K. Khanna, P. Kumar, R.K. Chaturvedi, K.C. Gupta, Trans-blood brain barrier delivery of dopamine-loaded nanoparticles reverses functional deficits in parkinsonian rats, ACS Nano. 9 (5) (2015) 4850–4871.

[27] J. Wu, L. Cao, Y. Liu, A. Zheng, D. Jiao, D. Zeng, X. Wang, D.L. Kaplan, X. Jiang, Functionalization of silk fibroin electrospun scaffolds via BMSC affinity peptide grafting through oxidative self-polymerization of dopamine for bone regeneration, ACS Appl. Mater. Interfaces. 11 (9) (2019) 8878–8895.

[28] Y. Ha, X. Ma, S. Li, T. Li, Z. Li, Y. Qian, M. Shafiq, J. Wang, X. Zhou, C. He, Bone microenvironment-mimetic scaffolds with hierarchical microstructure for enhanced vascularization and bone regeneration, Adv. Funct. Mater. 32 (2022) 2200011.

[29] C. Xu, Y. Chang, Y. Xu, P. Wu, C. Mu, A. Nie, Y. Qu, D. Duan, X. Guo, Z. Liu, J. Wang, Z. Luo, Silicon-phosphorus-nanosheets-integrated 3D-printable hydrogel as a bioactive and biodegradable scaffold for vascularized bone regeneration, Adv. Healthc. Mater. 11 (2022) 2101911.

[30] P.S.J.S. Long Bai, Bioactive elements manipulate bone regeneration, Biomater. Transl. 4 (2023) 248–269.

[31] T. Deng, D. Gao, X. Song, Z. Zhou, L. Zhou, M. Tao, Z. Jiang, L. Yang, L. Luo, A. Zhou, L. Hu, H. Qin, M. Wu, A natural biological adhesive from snail mucus for wound repair, Nat. Commun. 14 (2023) 396.

[32] L. Teng, Z. Shao, Q. Bai, X. Zhang, Y.S. He, J. Lu, D. Zou, C. Feng, C.M. Dong, Biomimetic Glycopolypeptide hydrogels with tunable adhesion and microporous structure for fast hemostasis and highly efficient wound healing, Adv. Funct. Mater. 31 (2021) 2105628.

[33] Q.Y. Zhang, J. Tan, K. Huang, R. Nie, Z.Y. Feng, C.Y. Zou, Q.J. Li, J. Chen, N. Sheng, B.Q. Qin, Z.P. Gu, L.M. Liu, H.Q. Xie, Polyphenolic-modified cellulose acetate membrane for bone regeneration through immunomodulation, Carbohydr. Polym. 305 (2023) 120546.

[34] C. Huang, Q. Ye, J. Dong, L. Li, M. Wang, Y. Zhang, Y. Zhang, X. Wang, P. Wang, Q. Jiang, Biofabrication of natural Au/bacterial cellulose hydrogel for bone tissue regeneration via in-situ fermentation, Smart Mater. Med. 4 (2023) 1–14.

[35] Z. Ahmadian, A. Correia, M. Hasany, P. Figueiredo, F. Dobakhti, M.R. Eskandari, S. H. Hosseini, R. Abiri, S. Khorshid, J. Hirvonen, H.A. Santos, M.A. Shahbazi, A hydrogen-bonded extracellular matrix-mimicking bactericidal hydrogel with radical scavenging and hemostatic function for ph-responsive wound healing acceleration, Adv. Healthc. Mater. 10 (2021) 2001122.

[36] F. Wu, Z. Yuan, M. Shafiq, L. Zhang, M. Rafique, F. Yu, M. EL-Newehy, H. EL-Hamshary, Y. Morsi, Y. Xu, X. Mo, Synergistic effect of glucagon-like peptide-1 analogue liraglutide and ZnO on the antibacterial, hemostatic, and wound healing properties of nanofibrous dressings, J. Biosci. Bioeng. 134 (2022) 248–258.

[37] S. Pons, P. Jammet, S. Galmiche, A. Damecourt, D. Las, V. Blatière, D. Bessis, M. de Boutray, Nanofat and platelet-rich plasma injections used in a case of severe acne scars, J. Stomatol. Oral Maxillofac. Surg. 123 (2022) 248450828.

[38] S. Wang, H. Zheng, L. Zhou, F. Cheng, Z. Liu, H. Zhang, L. Wang, Q. Zhang, Nanoenzyme-reinforced injectable hydrogel for healing diabetic wounds infected with multidrug resistant bacteria, Nano Lett. 20 (2020) 5149–5158.

[39] P. Sun, Q. Zhang, W. Nie, X. Zhou, L. Chen, H. Du, S. Yang, Z. You, J. He, C. He, Biodegradable mesoporous silica nanocarrier bearing angiogenic QK peptide and dexamethasone for accelerating angiogenesis in bone regeneration, ACS Biomater. Sci. Eng. 5 (12) (2019) 6766–6778.

[40] H. Peng, T. Ling, Y. Zhang, T. Xie, X. Pei, K. Zhou, A. Chen, J. Chen, X. Zhu, X. Zhang, Z. Zhou, Nanowhiskers orchestrate bone formation and bone defect repair by modulating immune cell behavior, ACS Appl. Mater. Interfaces. 15 (7) (2023) 9120–9134.

[41] J. Li, J. Ma, H. Sun, M. Yu, H. Wang, Q. Meng, Z. Li, D. Liu, J. Bai, G. Liu, X. Xing, F. Han, B. Li, Transformation of arginine into zero-dimensional nanomaterial endows the material with antibacterial and osteoinductive activity, Sci. Adv. 21 (2023) eadf8645.

[42] S. Mcloughlin, A.R. Mckenna, J.P. Fisher, Fabrication strategies for engineered thin membranous tissues, ACS Appl. Bio Mater. 7 (2023) 2546–2561.

[43] A. Jin, Y. Wang, K. Lin, L. Jiang, Nanoparticles modified by polydopamine: working as "drug" carriers, Bioact. Mater. 5 (2020) 522–541.

[44] Y. Fu, L. Yang, J. Zhang, J. Hu, G. Duan, X. Liu, Y. Li, Z. Gu, Polydopamine antibacterial materials, Mater. Horizons. 8 (2021) 1618–1633.

[45] Z. Jin, L. Yang, S. Shi, T. Wang, G. Duan, X. Liu, Y. Li, Flexible polydopamine bioelectronics, Adv. Funct. Mater. 31 (2021) 2103391.

[46] H. Hemmatpour, O. De Luca, D. Crestani, M.C.A. Stuart, A. Lasorsa, P.C.A. van der Wel, K. Loos, T. Giousis, V. Haddadi-Asl, P. Rudolf, New insights in polydopamine formation via surface adsorption, Nat. Commun. 14 (2023) 664.